Proceedings of IMECE2004
ASME INTERNATIONAL MECHANICAL ENGINEERING CONGRESS
November 13–19, 2004, Anaheim, California USA

IMECE2004-60727

AN INNOVATIVE TECHNIQUE FOR BI-MATERIAL INTERFACE TOUGHNESS RESEARCH

John Jy-An Wang, Ian G. Wright, Ken C. Liu, Michael J. Lance
Oak Ridge National Laboratory, Oak Ridge, TN 37831-6171
Phone:(865)574-2274, E-mail:Wangja@ornl.gov
Roy L. Xu
Vanderbilt University, Nashville, TN 37235

ABSTRACT

A material configuration of central importance in micro-electronics, optoelectronics, and thermal barrier coating technology is a thin film of one material deposited onto a substrate of a different material. Fabrication of such a structure inevitably gives rise to stress in the film due to lattice mismatch, differing coefficient of thermal expansion, chemical reactions, or other physical effects. Therefore, in general, the weakest link in this composite system often resides at the interface between the thin film and substrate. In order to make multi-layered electronic devices and structural composites with long-term reliability, the fracture behavior of the material interfaces must be known. Unfortunately, none of the state-of-the-art testing methods for evaluating interface fracture toughness is fully conformed to fracture mechanics theory, as is evident from the severe scatter in the existing data, and the procedure dependence in thin film/coating evaluation methods. This project is intended to address the problems associated with this deficiency and offers an innovative testing procedure for the determination of interface fracture toughness applicable to thin coating materials in general. Phase I of this new approach and the associated bi-material fracture mechanics development proposed for evaluating interface fracture toughness are described herein. The effort includes development of specimen configuration and related instrumentation set-up, testing procedures, and postmortem examination. A spiral notch torsion fracture toughness test (SNTT) system was utilized. The objectives of the testing procedure described are to enable the development of new coating materials by providing a reliable method for use in assessing their performance.

1. Introduction

During the last decades, the technology of electronics has advanced very rapidly, introducing manufacturing and packaging techniques that led to extremely small components. Microelectro-mechanical Systems (MEMS) [1,2] evolved from the technology of silicon micro-fabrication, and introduced the concept of micro-sized mechanical "moving" components, with the attendant mechanics of materials problems. Multi-layered and composite systems, which often contain metal/ceramic interfaces, are widely used in industry, both in microelectronic packaging and as structural materials. Examples are thin film materials with particular electrical, magnetic, and optical properties that are used extensively in the micro-fabrication of integrated circuits, sensors, actuators [1,2]. In a completely different field, increasing the power and/or efficiency of propulsion systems requires them to operate at higher temperatures, and the point was reached several years ago where the materials considerations required to provide strength at high temperature are incompatible with those to provide environmental protection. As a result, such systems must rely on coatings or composite structures, in which the mechanical and chemical integrity of interfaces are critical to their successful application [3,4]. The need to maintain interfacial integrity at high temperatures under conditions of high heat flux, and the consequent effects on thermochemical stability and interdiffusion, it is difficult to obtain the combination of required properties

from a single material, so that coatings are used extensively [5-9]. These coatings comprise a thermally-insulating layer of ceramic together with a metallic layer intended to develop a specific, protective oxide film beneath the ceramic as well as to provide the means of securing the ceramic to the metallic substrate. [10, 11]

Also relevant is the mechanical behavior of these different types of films, which can range in thickness from nanometers to microns. Residual stresses and material discontinuities arise naturally from the deposition or growth processes used to produce these films, and further stresses may be imposed from thermal cycling in service and mismatch in coefficients of thermal expansion (which can be severe in the case of TBCs). These undesirable stresses and other physical effects due to service can lead to fracture, delamination, and other modes of damage initiated at the interface(s) [12-19]. Thus, the need to understand the processes that govern the mechanical properties of the interfaces between these dissimilar materials becomes important, since the mechanical properties of these interfaces ultimately control the reliability of the device and the performance of the composite structural material.

1.1 The Mechanics of Thin Film Materials

For the case of thin film materials and other small structures intended for electronic applications, interest is focused on the role of mechanical stress in defect nucleation and growth. Stress typically arises in such materials due to the constraint of epitaxy, a mismatch in coefficients of thermal expansion, or intrinsically as a result of growth processes. The simplest and most common configuration of this kind involving epitaxial structures is a thin layer grown onto a substrate, under circumstances where the lattice parameter of the layer material differs from that of the substrate by a small amount. The strain in the layer induced by epitaxy may be a by-product of material selection on some non-mechanical grounds, or it may be exploited to tailor the electronic properties of the film material. In either case, the stress associated with this strain provides a driving force for nucleation and growth of crystal defects, mainly dislocations and stacking faults.

In the electronics industry, the reduction of component size has been intensely pursued and the thickness of large-scale integrated circuit (LSI) device is reaching less than 1μm. Since the sub-micron components consist of the multi-layered films made of ceramics, intermetallic compounds and metals, the delamination at the interface becomes one of major failure modes in the processing and in service of LSI. Therefore, it is important in terms of reliability to evaluate the interface toughness between the thin films. Especially, the delamination crack usually initiates at the edge of thin films due to the stress concentration originated from the mismatch of deformation, namely the free edge effect

For the case of TBCs, the predominant failure mode appears to involve a cyclic displacement instability occurring in the thermally-grown interfacial oxide (TGO), (Evans et al., 2001; Gell et al., 1999; Johnson et al., 1998; Mumm et al., 2001; Ruud et al., 2001; Spitsberg et al., 2002; Wright and Evans, 1999). The instability happens because the TGO is a thin layer subject to large levels of residual compression. The compression is caused by a combination of growth strain (converting the Al in the alloy to Al_2O_3), and a low coefficient of thermal expansion that results in misfit with the metallic substrate upon cooling. The compressive stress reaches several GPa at ambient temperature (Karlsson and Evans, 2001; Tolpygo and Clarke, 2000). One of the mechanisms available to relieve the compressive stress is by means of out-of-plane displacement of the thin oxide layer, but this can locally disrupt the outer ceramic thermal barrier layer and lead to failure of the TBC system. There is a complex interplay of phase change and morphological developments in the growing oxide film, and modification of the properties of the oxide-substrate interface due to segregation of specific elements from the metallic substrate or the nucleation of voids. All of these result in time-dependent changes in the properties of the interface. On-going research is developing an improved mechanistic understanding of how such changes occur; the ability to link this understanding with the effects on the mechanical integrity of the interface could provide routes for increased stability, hence longer service life.

1.2 Theoretical and Experimental Development of Interfacial Mechanics

Bi-material systems with property mismatch are encountered in many advanced material and nano-technology development. A theoretical framework for analyzing the mechanics of fracture of dissimilar material interfaces was developed by Williams (1959), and subsequently expanded by many others, including Rice and Sih (1964), Erdogan (1965), Bogy (1970) and Huntchson and Suo (1992) [20-26]. A resurgence in the

interest for quantifying fracture behavior of bi-material systems, in terms of fracture toughness and fracture mode mixity, is evident from the works reported in many recent papers. Yet, both the fundamental mechanics, and experimental techniques capable of systematically characterizing such fracture, are incompletely developed, due to lack of appropriate testing procedures that can properly characterize the interfacial mechanical properties.

Experimental techniques typically used in bi-material interface research are double-cantilever beam tests, four-point bending tests, indentation techniques, and laser spallation [27-32]. The first two approaches can provide information regarding toughness evaluation, but the large uncertainty involved casts doubts regarding the validity of the test results. For example, in double -cantilever beam tests and four point bending tests, the interfacial crack generally does not propagate along the interface but often will kink out of the interface. In indentation technique, the test result is dependent on the indentation load, penetration depth, and specimen size and geometry. Moreover, the penetration depth during the indentation test is very difficult if not impossible to control, due to the sudden release of the compressive residual stress while the indenter penetrates through the thin film or coating. Furthermore, the indention technique requires very large plastic deformation to induce crack initiation, which is very likely to provide a non-conservative estimate of interface toughness. The laser spallation technique has been be used for estimating interface strength subject to high strain-rate. However, due to the nature of laser-induced kinetic energy stored in the lattice structure, and the consequence of instantaneous spallation, and complicated stress wave interaction at edges/boundaries, this technique also fails to provide quantitative interface toughness.

Spiral Notch Torsion Test methodology (SNTT), a 2002 R&D 100 Award winner, was developed by some of the present authors [33-39]. The applicability of SNTT has been verified for homogeneous materials, and for relatively large test samples (compared to the micrometer-level of thin films). Consequently, the applicability of this concept to thin film test samples of bi-materials needs to be validated. In this feasibility study, SNTT technology was modified for use in measuring the interfacial toughness of thin, protective oxide scales formed on a high-temperature alloy, Inconel® MA956 (nominally: Fe-20Cr-4.5Al-0.5Y_2O_3) after thermal traetment. In Phase I of the feasibility study, significant technical challenges were encountered both in developing the experimental procedures, and in the testing apparatus for the proposed configurations.

2. SNTT Approach for Toughness Evaluation

The SNTT methodology operates by applying pure torsion to cylindrical specimens machined with a notch line that spirals around the specimen at a 45° pitch angle. The pure torsion loading creates a uniform, equi-biaxial tension/compression stress field on each concentric cylinder, and the grooved line effectively becomes a Mode I (tensile) crack mouth opening, as illustrated in Fig. 1. It is not difficult to visualize that this rod specimen as a variant of a compact-tension specimen, having a width equivalent to the total length of the spiral notch. Compact-tension specimen testing has an inherent problem, which is lack of a means to uniformly distribute the applied load throughout the entire specimen thickness. This is because the stresses at and near the two free surfaces are anomalous, resulting in shear lip formation that often is discernible in fractured specimens. In contrast, the torque load acting on every cross-section along the rod specimen is the same and directly measurable, so that a plane-strain condition is achieved on every plane normal to the spiral groove.

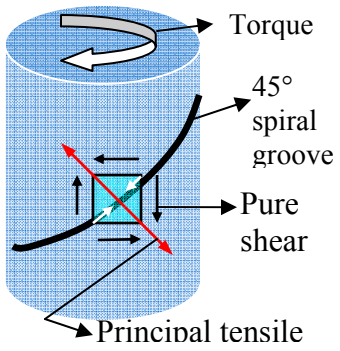

Figure 1. Schematic diagram of SNTT configuration.

Specimen miniaturization is an important option of the SNTT methodology, and serves the need of advanced materials development with limited material availability. Another feature of this technique is that the K_{IC} values determined are virtually independent of specimen size. In typical fracture toughness tests, the direction of crack propagation is unpredictable, and often deflects in zigzags or a thumbnail pattern, resulting in large data scatter. When a rod sample is twisted, the spiral notch provides a consistent location for cracking to start, and the pure torsion load ensures that the crack will advance perpendicularly toward the central axis of the test

specimen. This consistent cracking behavior has been verified from postmortem examination of fracture surfaces. Therefore, the SNTT methodology is expected to significantly reduce uncertainty in fracture toughness evaluation. Furthermore, the ability of SNTT to confine the plastic deformation within a thin plane provides the opportunity to investigate the interfacial material properties. In addition, SNTT provides an expedient means to investigate mixed-mode failure mechanisms by simply varying the pitch of the starter notch. The benefits of applying SNTT to thin film research are summarized below:

- The size effect in fracture toughness evaluation using SNTT is minimized; a long and uniform crack front will yield an accurate fracture toughness value, which is more likely near the statistical mean; thus, fewer test samples are needed to generate valid K_{IC}.
- For valid fracture toughness (K_{IC}) testing, conventional ASTM standards not only require fairly large specimens, but also require a fatigue precrack procedure to develop a sharp crack front. This is a very difficult task for interfacial fracture testing and the fatigue precrack itself results in a very large uncertainty in K_{IC} evaluation. For the SNTT approach, no fatigue precrack is needed for brittle materials such as ceramics or oxide layers and, as for the ductile interface, the fatigue crack growth is not expected to change course along the interface. Thus, the SNTT approach has several advantages for evaluating the intrinsic toughness at interfaces. This phenomenon will be further examined in this research.
- Mode mixity plays an important role in interface failure mechanisms. Recent publications indicate that a combination of Mode I and Mode III is more detrimental than Mode I alone for many materials of interest. For example, due to residual stresses, thin, thermally-grown thermal protective oxide layers seek mechanisms to relieve the compressive residual stress, which typically occurs by means of out-of-plane displacements. Thus, the combination effect of the out-of-plane Mode III (tearing shear mode) and Mode I needs to be assessed. The SNTT method provides an excellent tool for investigating combined Mode I and Mode III failure mechanisms.

3. Rationale of the Proposed Research

An example of an interface for which the information generated by the proposed technique would be extremely valuable is that between the metallic bond coating component of a thermal barrier coating, and the alumina scale that is deliberately grown on that bond coating to provide environmental protection, as well as to anchor the outer ceramic thermal barrier layer. Recall that the use of thermal barrier coatings (TBCs) has been pioneered on the airfoil surfaces of advanced gas turbine engines, where they are needed (in conjunction with internal cooling of the airfoils) in order to increase power and/or efficiency of operation, which is achieved by operating at combustion gas temperatures above the melting point of the alloys used for the airfoils,. The failure mode of TBCs typically involves crack propagation near to or along the interfaces between the ceramic and thermally-grown oxide (TGO), or between the TGO and the bond coating. When the characteristics of the ceramic layer are optimized, the weakest link in the TBC system will be at the TGO-bond coating interface. Our research was focused on the fracture behavior and toughness of such an interface, which is illustrated in Fig. 2.

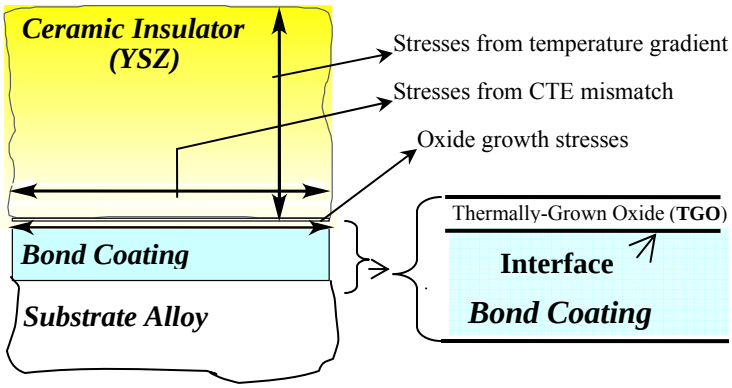

Figure 2. Schematice diagram of interface between bond coating and thermally-grown oxide

3.1 Basis of the Proposed Research Focus

Significant efforts have recently been made to model the mode of failure of TBCs in order to provide some life prediction capability, since unexpected failure of a TBC in service could have catastrophic results. Much of this effort has been focused on trying to understand the criteria for initiation of cracking, especially of cracking that leads to separation of the thermally-grown oxide scale from the bond coating. In addition to understanding the factors that govern the development of stress along the TGO-bond coating interface, especially from growth of the oxide and from coefficient of thermal expansion (CTE) mismatch during thermal cycling, techniques have

been developed to try measuring some of these parameters in situ. In particular, photo-stimulated luminescence spectroscopy has been used to measure the stress level and crystal phase of the alumina scale itself, and attempts are being made to derive correlations with the tendency for scale spallation (hence loss of the TBC), so that such techniques may be used for monitoring conditions in service.

The unequivocal measurement of the fracture parameters for the interface in question would provide the datum point against which all such in situ measurement techniques could be calibrated. Further, the ability to measure the fracture toughness of the interface would provide an unambiguous measure of the effectiveness of TBC developments intended to increase service life, and lead not only to longer life, but also to assured performance and lower costs.

4. Proposed Experimental Approach for Thin Film Interface Fracture Toughness Testing

The focus of this thin film interface research was the interface of a thin, protective oxide scales (alumina) formed on a high-temperature alloy, MA956®, and its substrate. The development of the testing procedure for thin films required a major upgrade of the SNTT specimen preparation and the SNTT methodology, both in experimental procedures and analytical evaluation. In Phase I, several configurations of proposed SNTT specimens were investigated. Two types of notch configurations, a V-shape and a square U-shape with different aspect ratios, were used. An acoustic emission device was utilized to detect the crack initiation.

4.1 The Proposed Thin Film SNTT Configuration

The conceptual design used for testing the thin film is illustrated in Fig. 3. A circular rod of alloy MA956, machined with a shallow spiral groove, was used as the baseline. This alloy was chosen for its ability to reliably form a uniformly thick, adherent surface film of α-alumina, which is very similar to that formed on bond coating alloys used with TBCs. Thus, the complication of using coatings was avoided. A 10-15 mm thick alumina scale was formed after oxidation in air at 1200°C for 4 hours.) This specimen design utilized a 45° pitch angle of the spiral groove under pure torsion to generate opening mode stress along the interface between the oxide and the alloy. The optional fatigue precrack procedure applied to the baseline MA956 sample was also investigated. A parameter study of notch geometry, such as V- or U-shape notches, and the depth of the notch, was conducted to determine the most suitable configuration for thin film testing.

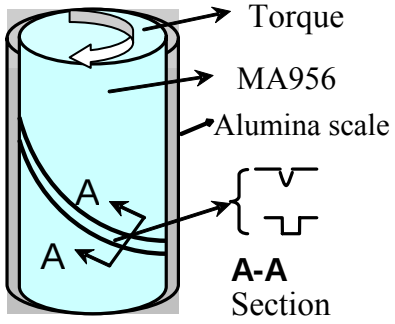

Figure 3. SNTT thin film sample.

4.2 Fracture Mechanism of SNTT Thin Film Specimen

The details of notch root geometry and the indicated failure initiation sites of an oxide MA956 SNTT sample are illustrated in Fig. 4. The shaded area of alumina scale indicates the region of thin film that is capable of transmitting resultant force of the principal stress induced

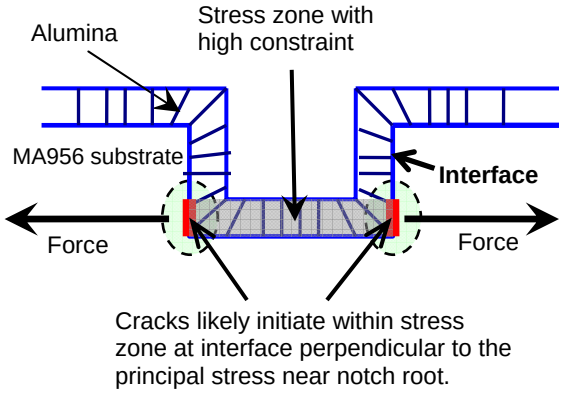

Fig. 4 Schematic diagram of notch root geometry and the associated crack initiation sites

by pure torsion loading. The orientation of the crack propagation for the proposed SNTT configuration is material dependent. With (1) thin film alumina scale of high hardness compared to that of substrate, and the compressive residual stress of the thin film (acting normal to the principal stress), and (2) potential notch root blunting or substrate yielding due to high tensile stress fields near the corner of the notch root, a crack is more likely to initiate from the corner of the notch root, and to propagate upward (in the orientation of Fig. 4) along the interface. After the threshold for crack growth along the interface (vertical in Fig. 4) has been exceeded, the compressive residual stress in the alumina will cause the

unsupported portion of alumina scale to buckle (due to the lack of lateral support from the substrate).

This hypothesized SNTT failure mode was confirmed from SEM examination of tested SNTT thin film samples. Thus, for a non-precracked, oxidized SNTT MA956 sample, cracking wis expected to initiate at the corner interface (at the bottom of the groove), and to grow upward along the interface, before it penetrates down into the substrate.

Due to the small dimensions of the thin film test sample, sensitive instrument control was needed, in particular, optical devices for measurement of subtle deformation. Additionally, acoustic and infrared instruments were needed to capture the onset of the crack initiation underneath the coating.

4.3 Test Sample Preparation

SNTT specimens were fabricated to the design shown schematically in Fig. 5 from a rod, 1-1/2-in. diameter, of alloy MA956, and from a 1/2" by 2" cross-section plate of a higher-Al variant (MA956HT, heat WBD0667).

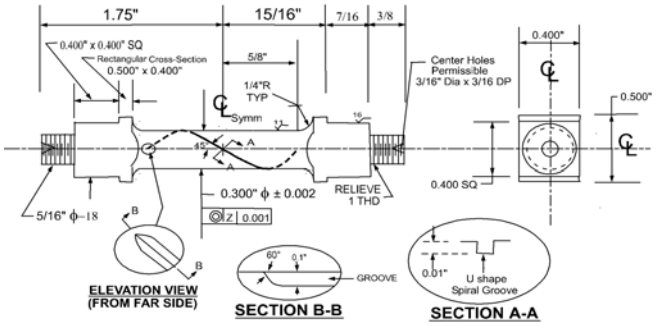

Fig. 5. SNTT thin film specimen design configuration

Both were in the recrystallized (1h at 1300°C) condition. A total of 10 SNTT spec were made, including five with V-notch grooves and five with U-notch grooves. While the size of the test specimen is optional, depending on the form of the available material, these specimens had a uniform gage section of 1-1/4" diameter, on which a complete lobe of a spiral groove with a pitch of 45° was machined. The squared end sections were made to transmit torque and the threaded ends for zero axial load control. Four SNTT specimens were used in the as-machined condition for calibrating fatigue precrack and evaluating fracture toughness of MA956.The other six SNTT samples were oxidized to grow an alumina surface film of thickness in the range of 7 to 12 μm (alloy MA956HT oxidizes more slowly than the standard alloy, and so grew a thinner film under the same oxidation conditions of 100 h in air at 1100°C). The alumina film was expected to be uniform in thickness, and to cover the entire rod surface including the spiral grooves. The corresponding material ID, groove geometry, baseline fatigue precrack, and heat treatment of the oxidized SNTT thin film specimens are listed in Table 1. Specimens with V- and U-type grooves were used in the thin film study.

Table 1. Specifications of SNTT Thin Film Samples

Specimen ID	Material ID	Notch Type	Baseline Precrack	Temp. °F / time hr
1	Heat 1[a]	V-1[c]	Yes	1100°C/100h
2	Heat 1	V-2[d]	Yes	1100°C/100h
3	Heat 1	U-1[e]	No	1100°C/100h
5	Heat 2[b]	V-1	Yes	1100°C/100h
7	Heat 2	U-1	No	1100°C/100h
9	Heat 2	U-1	Yes	1100°C/100h

[a]MA956-ANN 2300F; [b]MA956HT- Heat No:WBD0667.
[c]Type V-1: 0.015" deep, 60° vee; [d]V-2: 0.032" deep, 90° vee
[e]Type U-1: 0.016" deep and 0.0197" wide

5. Experimental Set-up and Test Results

Torsion tests were performed using a closed loop-controlled, electro-hydraulic, biaxial testing system, shown in Fig. 6. Test specimens were subjected to pure torsion controlled by LVDT and RVDT, in association with a high-sensitivity, biaxial load cell to maintain a zero

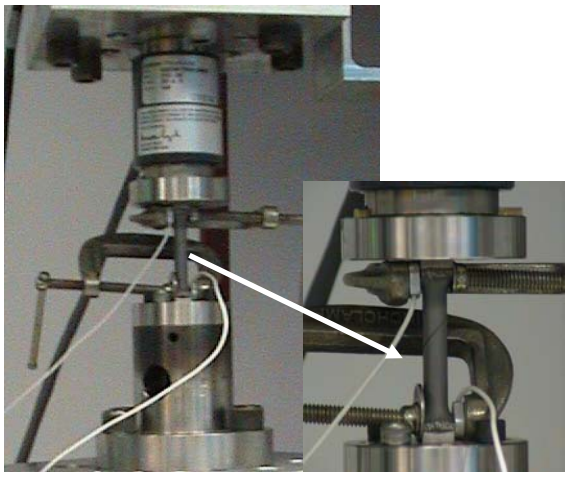

Fig. 6. Experimental set-up with acoustic emission sensors attached to the specimen.

axial load. In order to capture the onset of crack initiation , an acoustic emission device was used. Precracking for baseline MA956 specimens was accomplished by cyclic torsion, using the Haver sine wave form. The maximum torque used in precracking varies with materials and must be determined experimentally; normally 60~80% of the torque that generates the maximum shear stress around the specimen diameter will suffice. We did not use compliance to monitor the fatigue crack growth; instead, an approximate compliance function was used to estimate crack growth under loading and unloading sequences in torsion. To date, the closed-form solution for torsion compliance has not been developed. An exploratory procedure estimating load-displacement (or stress-strain) slope change at different phases of fatigue loading was adopted to estimate fatigue crack growth. The fatigue crack growth was measured by postmortem examination. In general, precracking was not needed for a brittle SNTT specimen, such as a ceramic. Also, for investigating interface cracking of an oxidized MA956 SNTT specimen, the precrack was considered to be redundant due to material discontinuity being a natural stress riser. However, in order to provide a comparison between the precracked baseline sample and the oxidized sample, two sets of SNTT baseline samples were prepared, one with a precrack and one without a precrack.

The fracture torque load at the crack initiation is needed as input for the interfacial fracture toughness evaluation, using a new SNTT analytical procedure. Determination of the torque at crack initiation required the use of several techniques concurrently, due to the micro-scale of oxide thickness. In recent years, infrared (IR) imaging has been applied successfully for detecting and monitoring fatigue crack growth. However, due to the highly insulating nature of the alumina film, the surface temperature profile of the SNTT oxide sample revealed from IR imaging was not useful for detecting or determining evolution of an interfacial crack underneath the alumina film. The acoustic emission technique, provided very consistent and distinct signals during the fracture test.

5.1. Baseline Fracture Toughness Experiment

Due to limited availability of alloy MA956, only four SNTT samples were used for exploring the fatigue precrack and fracture behavior for the as-received (non-oxidized) alloy. Of the three SNTT MA956 specimens used for evaluating the fatigue precrack procedures, all fractured during the exploration of the fatigue precrack testing procedure. This fatigue precrack procedure was then used to precrack some of the SNTT baseline samples. One sample intended to measure the fracture toughness of MA956 failed at 32 N-m with 0.06 inch deep crack. Instead, the fracture toughness data were estimated from the earlier SNTT fracture toughne ss data for A302B steel, with a/W ratio (crack length to diameter ratio) at about 0.4. The estimated toughness of the as-received MA956 material was about 68.36 MPa√m.

Fig. 7 Fractured SNTT samples.

5.2 Evaluation of Residual Stress of Thin Film Coating Material

5.2.1 Thin Film Stress Evolution

Since the oxide film grown by oxidation of the surface of alloy MA956 has a greater volume than that of the metal consumed, stresses invariably develop between the oxide and the underlying alloy. Further, the CTE of MA956 is significantly higher than that of alumina (IGW, 2001), providing a further source of stress during heating and cooling. There is a prevailing consensus that failure of an oxide film occurs when the stored elastic strain energy in the scale (the product of the scale thickness and the square of the stress) reaches a critical value. Therefore, the stress state in an oxidized scale is an important parameter in predicting the loss of integrity of the scale, and hence in assessing the long-term protection afforded the underlying alloy. Two general approaches have been used to describe the generation of stresses during oxidation. The first, suggested by Norin (1975), attributes the stress to epitaxial mismatch during the growth of a scale that mimics the orientation of the substrate. The second is a lateral growth model proposed by Rhines and Wolf (1970); the new oxide is presumed to form at the grain boundaries of the growing scale. The latter generally results in a compressive growth stress in the

scale that, unless relaxed by diffusional flow, will increase as the film thickness increases with continuing oxidation. The combinations of cation and anion defects that can lead to lateral growth of an oxide have been classified by Atkinson (1982).

5.2.2 Fluorescence measurements

The technique of Cr^{3+} fluorescence piezospectroscopy was used in this study to measure the stress in the α-alumina film formed by thermal oxidation. Three types of information concerning the scales can be obtained from the fluorescence measurements: the strain from the piezospectroscopic shift of the R-lines; the strain gradient through the oxide thickness from the broadening of the R-lines; and the crystallographic texture of the oxide film from the intensity ratio of the two R-lines. Measurements of the Cr^{3+} R-line fluorescence were made by exciting the oxide using an argon-ion laser operating at 514 nm. The laser was focused onto areas of interest with an optical microprobe. The excited fluorescence was collected along the same optical path. The fluorescence spectrum was dispersed using a triple-grating spectrometer equipped with a liquid nitrogen cooled CCD detector. The fluorescence line frequencies and widths were obtained by fitting spectra to double pseudo-Voigtian functions, one for each of the R-lines. All measurements were made at room temperature.

Table 2 shows the average hydrostatic stress collected from the thermally-grown α-Al_2O_3 scale from both the bulk (far away from the groove) and within the groove. The bulk stress varies slightly between samples which are due to different heating conditions. Average measurements collected within the groove show less stress and more stress variation than the bulk measurements which is most likely caused by the alumina scale spallation and interfacial cracking in this area. Stress measured in the bottom corner of Specimen 9 was much lower than all the other measurements because the scale was completely delaminated (but still intact) in this region. Figure 8 shows a residual stress profile across the U-groove site of Specimen No. 7 before the torsion test, and from Specimen No. 3 after the torsion test. The scan profile region spans from near the middle of the bottom groove, through the corner, up along the side-wall to the top edge of the corner (orientation as in Fig. 4). Even though Specimen No. 3 and No. 7 were made from MA956 and 956HT, respectively, the residual stress profiles were very similar, which may indicate that the majority of the thin film is are still intact after the torsion test. The estimate residual stress from the bulk and side of the U-groove of Specimen No. 3 was used as input for the boundary condition of the SNTT finite element model analysis.

Table 2. Residual Stress Estimated From Fluorescence Measurements

Specimen ID-Groove shape	Location	Hydrostatic Stress (GPa)	St. Dev.
1-U	Bulk	-3.58	0.03
2-V	Bulk	-3.49	0.03
3-U	Bulk	-3.66	0.01
	Groove/Bottom	-2.59	0.14
	Groove/Corner	-2.50	0.33
	Groove/Wall	-2.71	0.17
5-V	Bulk	-3.85	0.01
7-U	Bulk	-4.02	0.02
9-U	Bulk	-3.92	0.02
	Groove/Bottom	-2.68	0.08
	Groove/Corner	-0.27	0.01

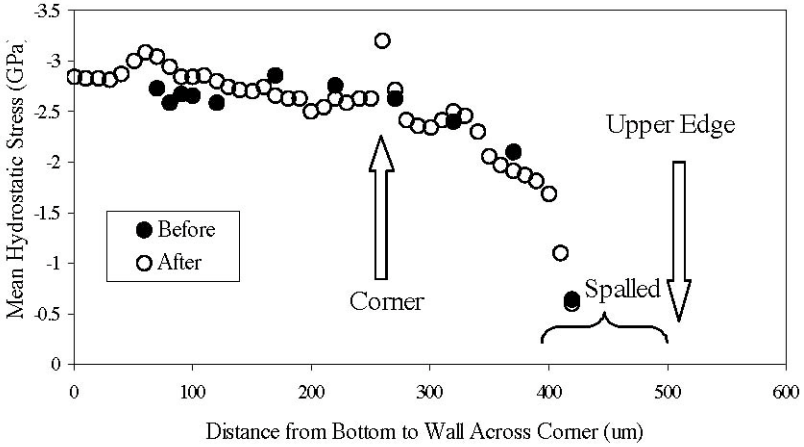

Figure 8. Residual stress profile across U-groove from Specimen No 7 before the torsion test, and from Specimen No. 3 after the torsion test.

5.3 Postmortem Examination of Oxide SNTT Specimens

5.3.1 Initial Visual Inspection

Initial visual examination was made following the

oxidation treatment of the SNTT samples. It appeared that the alumina scale at the top corner (see Fig. 9) of the V- or U-groove sites were all spalled, while the alumina scale remained intact on the rest of the SNTT samples. The residual stress distribution near the U-groove site is shown schematically in Fig. 9. For a thin, thermally-grown oxide, normal stress is not usually a concern except at the sites near delamination, such as at free edges. As indicated above, biaxial compressive residual stress fields exist within such films as a result of growth stress, and stress induced by CTE mismatch, which is a function of temperature and cooling rate, film thickness, etc. The out of plane normal stress typically does not exist, or is very small, for a flat plate with a relatively thick substrate. The stress fields of a thin film can be characterized as equal bi-axial stress fields, and estimated from hydrostatic pressure obtained from a nondestructive evaluation, such as Cr^{3+} fluorescence piezospectroscopy technique. As for the case considered here, a circular rod with notch may present a different problem compared to a flat surface. However, the above condition can still be hold for a curved surface with a curvature that is much larger than the thin film thickness. In our specimen design with a 0.15 inch diameter, the correspondence curvature is much larger than the film thickness at 10 μm range. Thus, the issue regarding residual normal stress still holds for a majority of the cylinder surface, except at the U-groove. Due to lack of information regarding spallation in real time, the possible cause of the alumina spallation at the top corner of the U-groove are listed below, with reference to Fig. 9.

It is well known that the free edge of a thin film can act as a site for delamination. In Fig. 9, Corner A is adjacent to two perpendicular thin film layers. The top corner of the substrate does not posses the characteristics of a free edge. From the point of a physical singularity and the surface slope discontinuity at a corner, it will be difficult to form a thin film with a well organized and orientated columnar structure, and subsequently to maintain the integrity of the thin film and its bonding with substrate during cooling. Furthermore, considering the residual stress distribution during cooling, as illustrated in the lower portion of Fig. 9, the tensile residual stresses of the substrate will have a tendency to pull the corner of the substrate away from its original position in a diagonal direction, while the compressive residual stress in the film has a tendency to push the alumina film away from the top corner of the substrate, also in a diagonal direction. It is not difficult to visualize that, with increasing residual

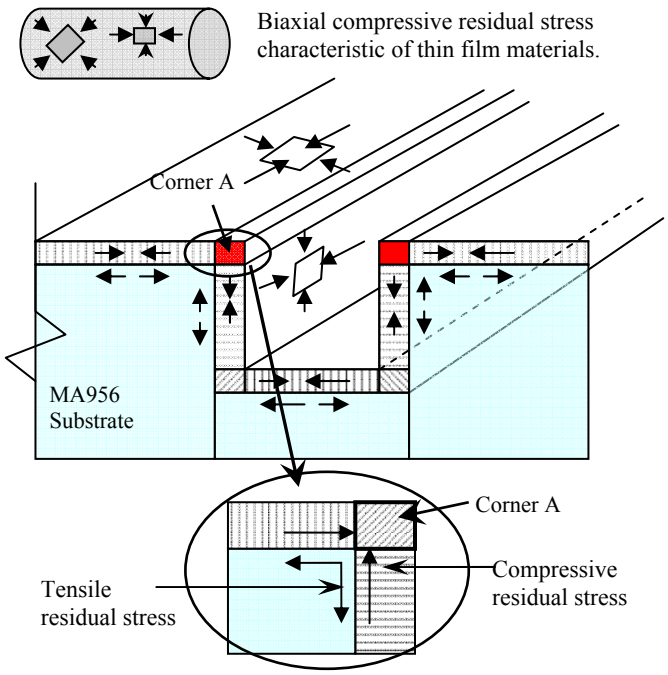

Fig. 9 Schematic diagram of residual stress fields near the U-groove site.

stress during cooling, the combined effect of tensile and compressive residual stresses at the corner will eventually detach the alumina film at the top corner of the U-groove.

5.3.2 Surface Examination of As-machined SNTT Samples

After the initial visual examination of the SNTT samples, the area around the spiral groove were also examined in detail by optical microscopy. This revealed the surface finish of the test samples to be fairly rough, especially at the spiral groove sites for Specimen Nos. 2 and 5. The surface roughness may have been due to machining performance, or to the machining properties of alloy of MA956. Microscopic surface images for typical V-groove SNTT samples are shown in Fig. 10 (for Specimen No. 1). Significant surface flaw sites were revealed around the V-groove in Specimen No. 5, including chipped edges and a wavy groove bottom (Fig. 11). Figure 12 shows two shallow grooves on both V-groove walls for Specimen No. 2; these were thought to be due to cutting errors during machining.

Surface images of typical U-groove sample (Specimen No. 9) are shown in Fig. 13. U-grooves seem to have less machining damage compared to that of V-grooves.

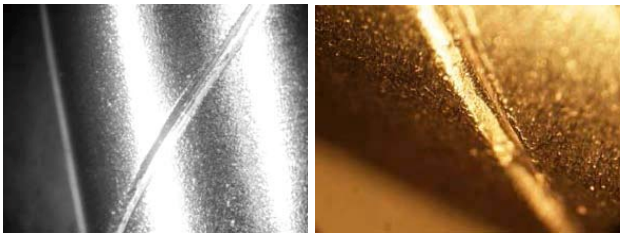

Fig. 10. Typical as-machined V-groove (Specimen No. 1).

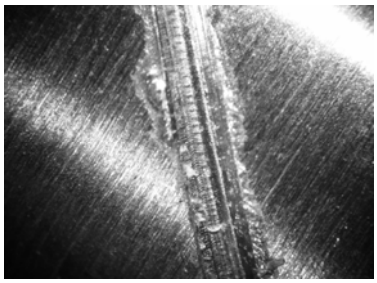

Figure 11. V-groove cutting flaw sites in specimen No. 5.

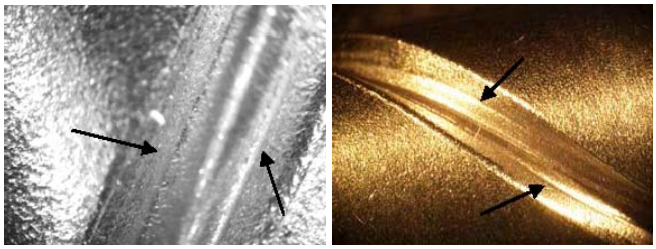

Figure 12. Cutting discontinuity (arrows) on both as-machined V-groove walls (Specimen No. 2)

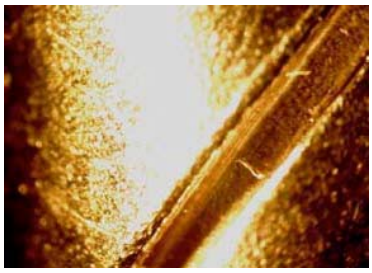

Figure 13. Typical appearance of as-machined U-groove (Specimen No. 9).

5.3.3 Surface Examination Oxidized SNTT Samples before Torsion Test

Plan views of the surfaces of oxidized U-groove SNTT specimens Nos. 3, 7, 9 shown in Figs. 14-16, show that the alumina scales had spalled from both the top corners of U-groove. The scale on Specimen No. 9 was thinner than that on Specimen No.3; shiny residues also were visible at the bottom of the groove. The difference of thin-film thickness between Specimens No. 9 and No. 3 was due to the different baseline materials, MA956 and 956HT, used to manufacturer these two samples. Plan views of the surfaces of oxidized V-groove SNTT specimens also show that the alumina scales had spalled from both the top corners of V-groove.

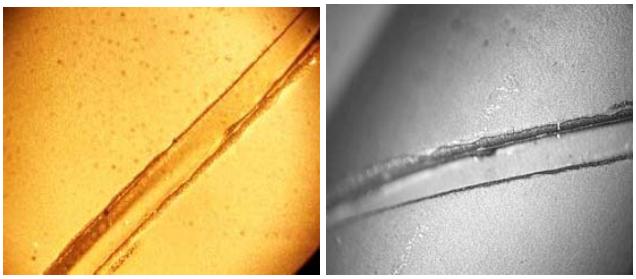

Figure 14. Views from south and north edges of U-groove on Specimen No. 3 (not pre-cracked).

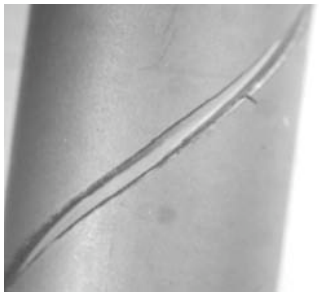

Figure 15. Specimen No. 7 (U-groove, not pre-cracked) after oxidation

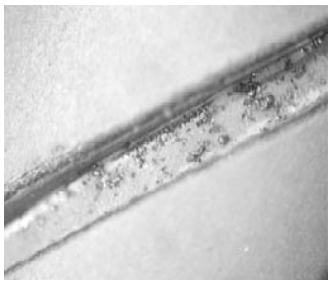

Figure 16. Specimen No. 9 (U-groove, pre-cracked) after oxidation

5.3.4 Examination of Oxidized SNTT Samples After Torsion Testing

5.3.4.1 Specimens with U-Section Grooves

Not Pre-Cracked

Figures 17-20 illustrate the fracture and spallation sites of the alumina scale as indicated with arrow marks for specimen Nos. 3 and 7 after torsion testing. The majority of the alumina scale at the bottom of the spiral groove appeared to be intact. A crack along the edge of the

bottom corner of the spiral groove on specimen No. 3 is shown in Figs. 17 and 18(a). A more detailed view of the alumina scale spallation at the bottom corner of the groove is shown in Fig. 18(b). A similar scale cracking and spallation site at the bottom of the groove on Specimen No. 7 is shown in Figs. 19, 20. There was no damage apparent at the bottom of the U-grooves in the as-machined samples, prior to oxidation.

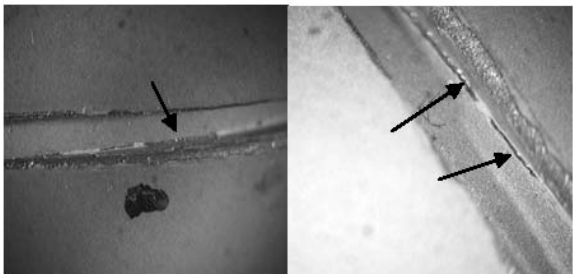

Figure 17. Scale spallation sites after torsion testing (Specimen No. 3)

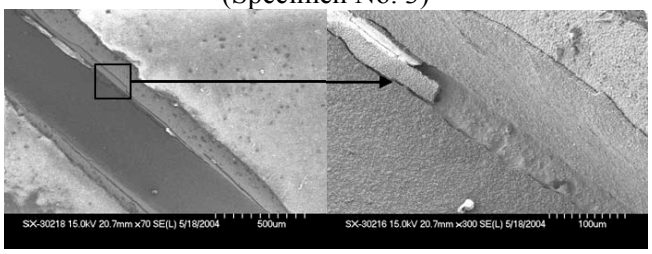

(a) (b)

Figure 18. Scale spallation at the bottom corner of Specimen No.3.

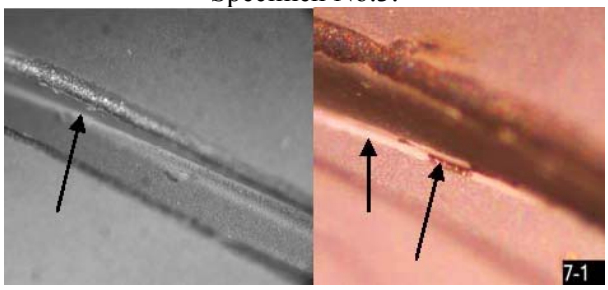

Figure 19. Scale delamination and spallation sites after torsion testing (Specimen No. 7).

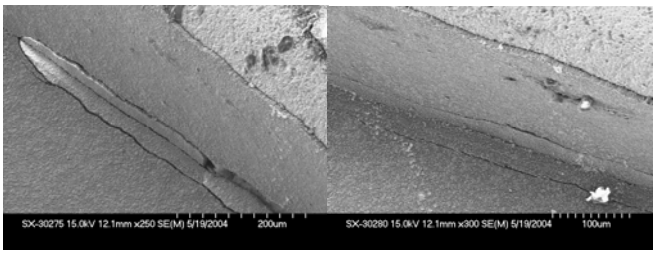

Figure 20. Scale crack and spallation sites along the bottom of the U-groove after torsion testing (Specimen No. 7).

Pre-Cracked

In contrast, on the pre-cracked samples (Nos. 1 and 9) a large portion of the alumina scale near the center region of the spiral groove appeared to be delaminated from the substrate. The scale failure sites on Specimen No. 1 are shown in Figs. 21 and 22; the scale appears to be spalled or delaminated in the middle section of the groove. The alumina spallation sites near the center did not exhibit an 'oxide footprint' pattern (Figure 22b,d), compared to the spallation sites at the top corner of the U-groove, suggesting that the oxide was not in contact with the alloy at the conclusion of the oxidation treatment. The wide spread damage was most likely attributable to the pre-cracking of the samples. Figure 22(b) shows a large cavity beneath the alumina scale, possibly associated with an original machining defect in the groove.

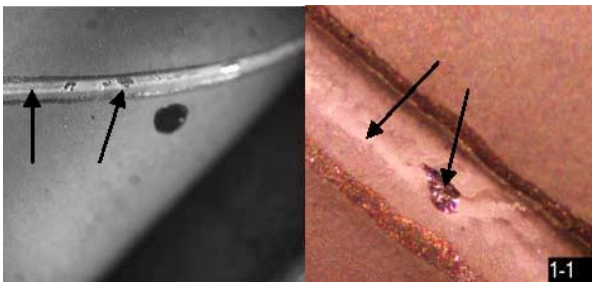

Figure 21. Scale spallation and delamination sites after torsion testing (Specimen No. 1)

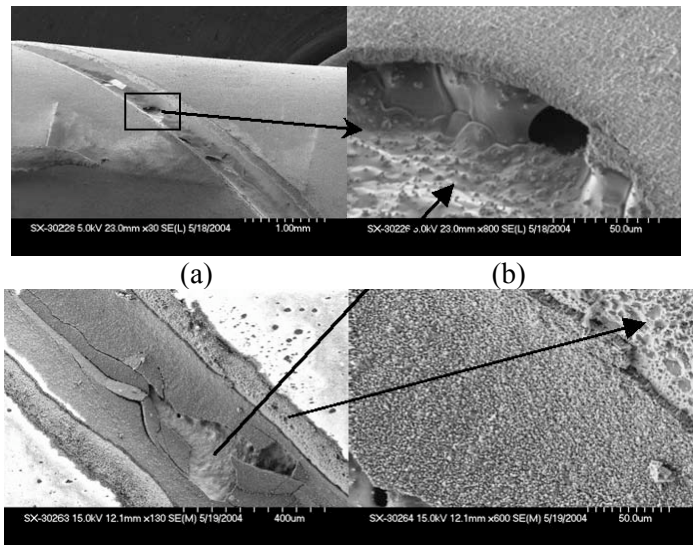

(a) (b)

(c) (d)

Figure 22. Unusual features at spallation sites in the U-groove on pre-cracked Specimen No. 1, after torsion testing

Comparison of the oxide on the U-grooves of Specimens

No. 9 and No. 7 (not pre-cracked), shown in Figs. 23 and 19, indicates fewer spallation sites on the non-pre-cracked specimen. This delamination on the pre-cracked specimens may have resulted from the development of an oxide wedge at the tip of the pre-crack sites during oxidation. Figure 24(a) shows typical U-groove spallation and crack sites on Specimen No. 9, which are similar to those of non-precracked samples, but more extensive. Details of the alumina scale spallation site at the bottom corner of U-groove are shown in Figure 24(b), and Figure 24(c) shows typical crack sites near the bottom corner of the groove. Figure 24(d) shows the external features of the alumina scale.

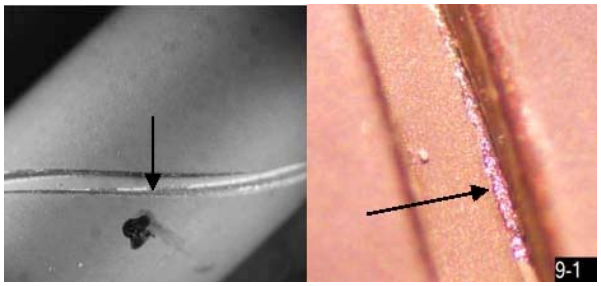

Figure 23. Scale spallation in groove after oxidation (Specimen No. 9, pre-cracked).

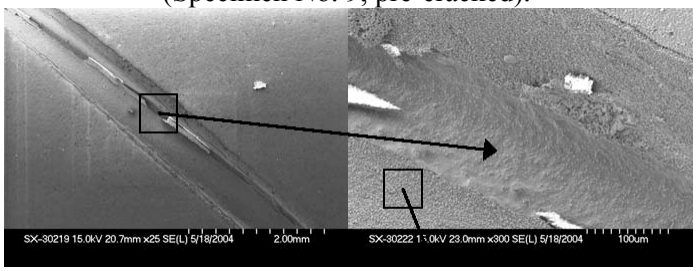

(a) (b)

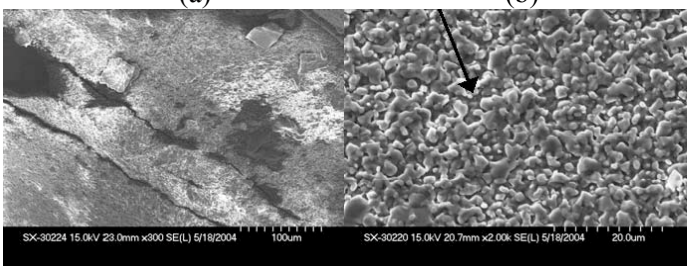

(c) (d)

Figure 24. Spallation sites (a) top view and (b) bottom corner, (c) alumina crack sites at bottom corner, and (d) plan view of adherent scale (Specimen No. 9).

5.3.4.2 Specimens with V-Section Grooves

Two parallel spallation lines were observed on pre-cracked specimen No. 2 (Fig. 25), which are consistent with the flaw sites identified on the baseline sample. Also, in Fig. 25a crack line can be seen near the root of the V-groove, and some scale delamination sites also are visible near the bottom of the spiral groove (Figs. 25b and 26). Figures 27 and 28 illustrate a scale spallation pattern on pre-cracked specimen No. 5 that corresponded to the rough, as-machined surface shown in Fig. 13, and demonstrates the detrimental effects of poor initial surface quality on the structure and adhesion of the oxide scale.

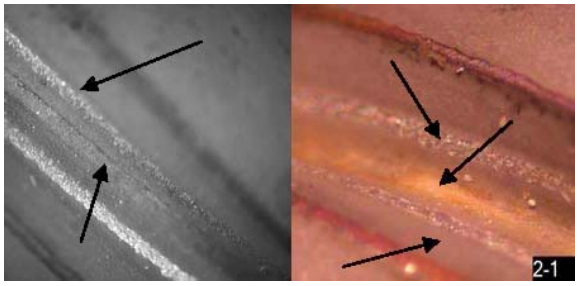

Figure 25. Fracture site (left) and spallation and delamination sites (right) after torsion testing (Specimen No. 2; pre-cracked).

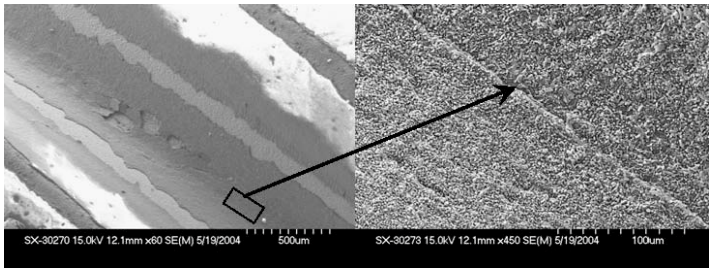

Figure 26. Scale spallation and crack sites on Specimen No. 2.

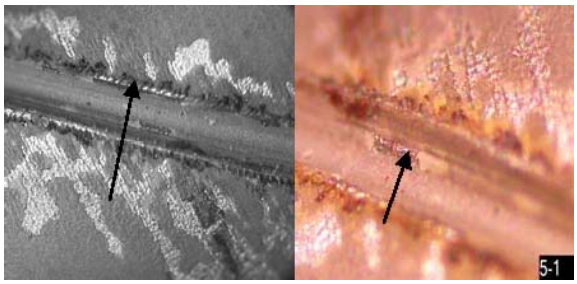

Figure 27. Scale spallation site of precracked Specimen No. 5 after torsion testing

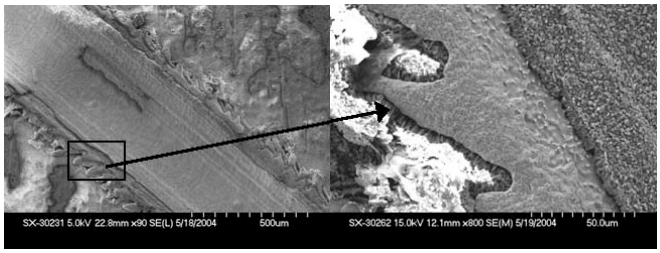

Figure 28. Irregular alumina formation near the edge of V-groove due to machining flaw at the edge of the spiral groove on Specimen No. 5.

5.3.5 Examination of Oxidized, U-Grooved SNTT Specimens Fractured <u>After</u> Torsion Testing

In order to further examine the surface features beneath the oxide film, a control cycle fatigue procedure was used to fracture U-grooved SNTT Specimens No.1 (pre-cracked) and No. 7 (not pre-cracked) to allow access for SEM imaging of the side wall, the bottom of the spiral groove, and the bottom corner along the spiral groove.

5.3.5.1 Pre-Cracked Specimen

Figure 29 shows alumina spallation sites near the top edge of the spiral V-groove from the fractured Specimen No. 1. The scale over region A in Fig. 29 apparently was not in contact with the alloy (lack of 'oxide footprints,' so that spallation occurred during cooling following oxidation. The remaining spallation sites in Fig. 29 apparently formed during the fatigue fracture test, since the alloy surface exhibits extensive 'oxide footprints,' signifying an adherent oxide. Figures 30-31 show details of spallation sites at the bottom of the spiral groove. The oxide appears to have bridged areas containing deep voids; the lack of 'oxide footprints' on the flat surface between the voids, and the smooth contours of the voids themselves indicate that these constituted a very large cavity beneath the original scale. The fact that the oxide was in contact only with the tops of the 'pillars' shown in Fig. 30 (Region 'B') and Fig. 31, and yet grew with the expected columnar grain structure to a uniform thickness is surprising, and suggests that transport of Al vapor species across the cavity was faster than oxygen diffusion through the oxide. This spallation site is near the location of the fatigue pre-crack that was formed at the bottom of the U-groove prior to oxidation.

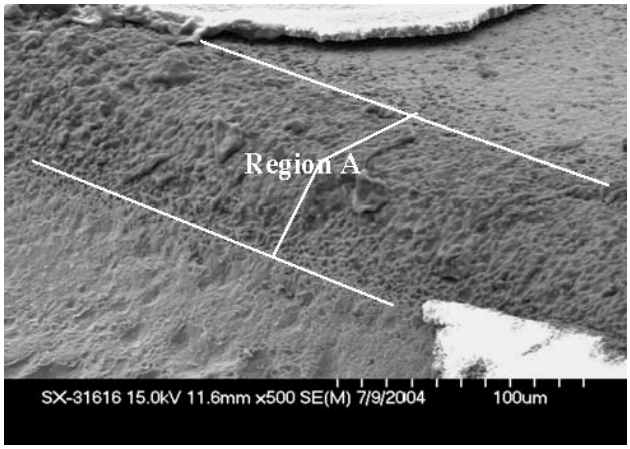

Figure 29. Scale spallation sites at near the edge of groove on pre-cracked Specimen No. 1.

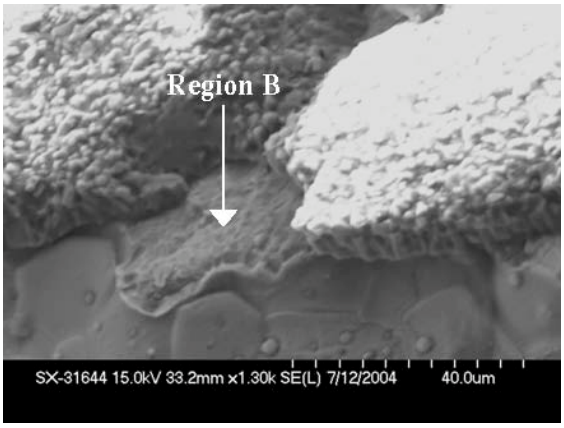

Figure 30. Region B reveals a location where the alumina scale was adherent at temperature (Specimen No. 1).

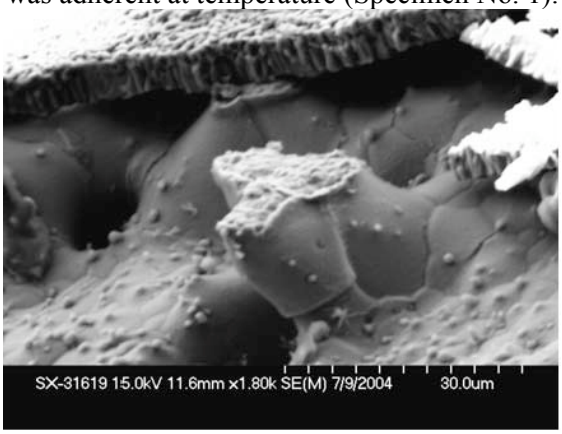

Figure 31. A pillar-like structure near the fatigue pre-crack site on Specimen No. 1.

5.3.5.2 Not Pre-Cracked Specimen

Figure 32 illustrates scale spallation sites on right side wall and the bottom portion of the U-groove on Specimen No. 7. Spallation typically was focused at the intersection of the side-wall and bottom of the U-groove (Fig. 32b). The scale on the rest of the side-wall and bottom of the groove remained intact, indicating that good bonding between the alumina scale and the substrate still remains even after numerous torsion fatigue cycles.

Figure 33 shows two views of the fracture faces of the adherent scale on the bottom flat portion of the U-groove, near the site of the overall fatigue failure. The cross section of the oxide appears typical of the normal scale grown on this alloy. However, there is also a distinct layer of different appearance from the oxide and alloy located between the alumina scale and the substrate, as indicated by the arrows. Further examples of the layer from the corner between the wall and bottom of the groove are shown in Fig. 34, where the bottom section of the groove was broken away when the specimen

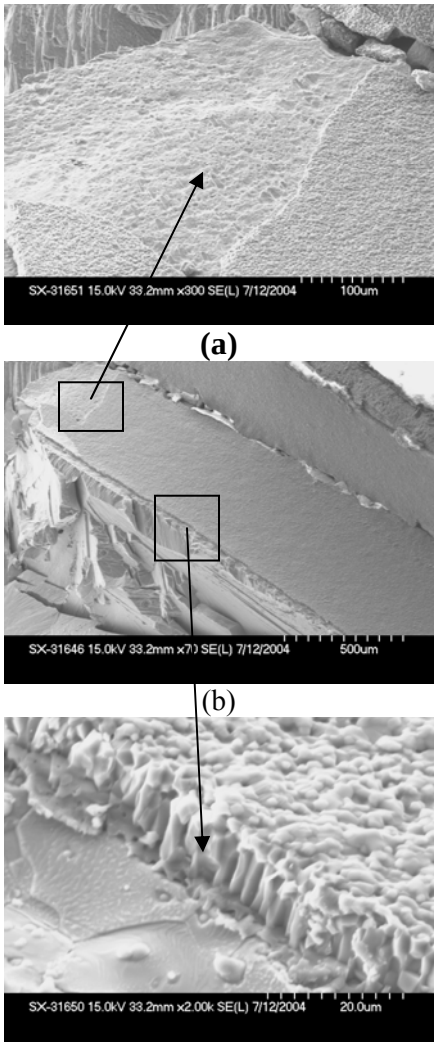

Figure 32. Details of spallation sites at the bottom and bottom corner are shown in (a) and (c); corner/ edge of U-groove bottom as shown in (b); (Specimen No. 7; not pre-cracked).

fractured. The finding of this underlying structure in SEM was purely by chance from the fractured No. 7 SNTT specimen with a proper viewing angle. Since the oxide has grown on this layer in the expected way, the layer is clearly MA956. The proximity of the layer and the structures that resemble the 'pillars' noted earlier (Fig. 31) suggests some connection: the smooth sides of the 'pillars' and the 'fracture face' of the layer, and the absence of 'oxide footprints' around the base of the 'pillars' further suggest the presence of a larger cavity between the unidentified layer and the alloy during the oxidation process. Possibly, the layer may be associated

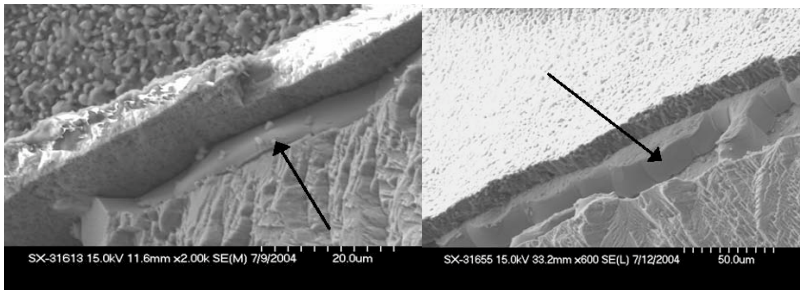

Figure 33. The fracture reveals a distinct, unidentified layer between the alumina scale and the substrate as indicated arrows in (a) the view from underside of the bottom flat of U-groove and (b) view from the top of the bottom corner edge of U-groove (Specimen No. 7).

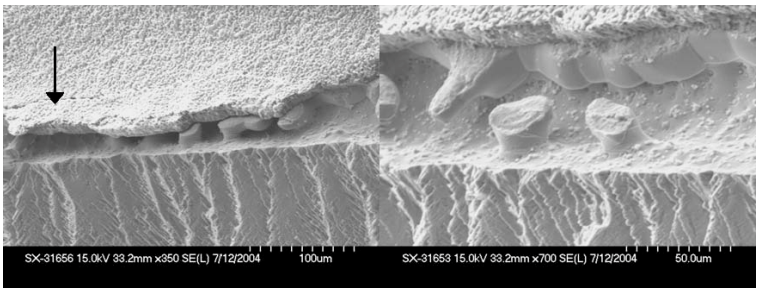

Figure 34. Complex defect sites at the bottom corner of U-groove from the fractured Specimen No. 7

with gross machining that remained attached to the surface. However, the uniform thickness of this distinct layer throughout the observed U-groove section (both at the bottom and on the side-wall of U-groove) may indicate that the above hypothesis is not likely. Thus, it is not clear what is the root cause of formation of this distinct layer. Further investigation is needed to clarify the fundamental forming mechanism of this phenomena.

The topography shown in Fig. 34 reveals a complicated structure near the bottom of the side-wall of U-groove, such as pillar-like and void structures. These phenomena may well be due to the violent fatigue fracture event of the fractured No. 7 SNTT sample. Nevertheless, the observed structure clearly indicates that the potential defects exist at near the bottom corner of the U-groove. This defect formation phenomena is likely due to high intensity stress fields existing at the bottom corner of U-groove. This high stress field is the result of the interaction between the geometry constraint of a U-groove, oxide growth stresses, and the high residual stresses associated with the formation of the alumina scale. For a brittle material, the fatigue precrack procedure is not required while utilizing the SNTT

approach to evaluate a valid fracture toughness, where a shallow notch or flaw will be sufficient. Furthermore, to induce a precrack at the bi-material interface is an extremely difficult task, if not possible. With these potential flaw sites existing at near the bottom corner of U-groove shown in Fig. 35, it sufficiently provides a crack starter or crack initiation site for a valid SNTT fracture toughness evaluation.

5.3.5.3 Oxide Wedging in V-Grooved Specimens

A schematic diagram of the formation of such a wedge is illustrated in Fig. 35, where the precrack was initially closed, but reopened during oxidation. Consequently, the alumina scale grew into the crack to form an oxide wedge. Upon cooling or loading, this oxide wedge will provide a driving force to extend the crack further into the alloy substrate. This crack growth phenomenon beneath the alumina scale is thought to be the main cause of the observed scale delamination and spallation at the center section of precracked V-grooved SNTT samples.

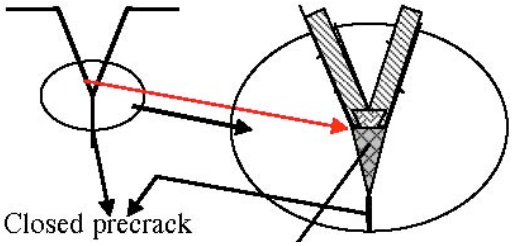

Figure 35. Schematic diagram of the formation of an oxide wedge.

5.4 Test Results From SNTT Thin Film Fracture Test and Acoustic Emission Detection

5.4.1. Acoustic Emission Testing

A material under stress accumulates energy, and sudden deformation produces elastic waves and generates acoustic emission (AE) signals. The stress and the associated strain can be tensile, compressive, or shear so that, under stress a material expands, contracts and/or shears. Up to the yield point, strain is elastic, but is permanent or plastic after yielding. Acoustic emission is associated with permanent strain. Therefore, AE can be defined as transient elastic waves generated by the rapid release of energy within a material. With AE equipment one can "listen" to the sounds of crack growth, and many other modes of active damage in the stressed materials. The ideal acoustic emission source generates spherical waves, but in real structures the propagation is affected by surfaces. An acoustic emission system, LOCAN 320, was used in this research for detecting crack initiation in oxidized SNTT samples under torsional loading. LOCAN 320 is a computerized system that performs AE signal measurements and stores, displays, and analyzes the resulting data in real time. The acoustic signals from the loaded structure are converted into electrical signals by the sensors, amplified to useable voltage levels by the preamplifiers and measured in two-channel computerized modules known as Independent Channel Controllers (ICCs). Each AE source event in a structure may be detected by one, two, or more channels; detection on any one channel constitutes a "hit," so that each event may produce one or several hits. Each AE signal (hit) is described in terms of its features, as shown schematically in Fig. 36, which includes:

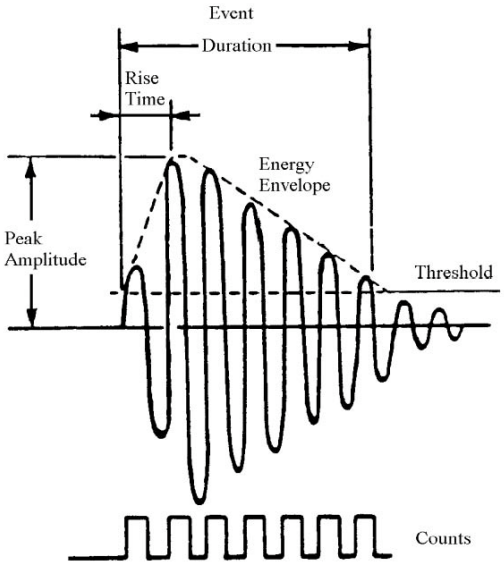

Figure 36. The AE waveform characteristic

(1) Hit−a burst acoustic emission signal,
(2) Time−the time of detection signal, in μ sec,
(3) Rise time−the time from the first threshold crossing to the peak, in μ sec,
(4) Duration−the time from the first to the last threshold crossing, in μ sec,
(5) AE Counts−the number of times the acoustic emission signal crosses the threshold,
(6) AE Count to Peak,
(7) Energy−area under the signal envelope,
(8) Average Frequency,
(9) Threshold level, in dB,
(10) Peak AE Amplitude −the peak voltage of acoustic emission signal (usually logarithmic), in dB.

The time, rise time, energy, amplitude, and AE counts are useful in identifying the crack initiation and its characteristics during a torsion test. For example, the AE amplitude is useful for comparing the relative distance of source sites from the sensors, since amplitude attenuation in proportional to distance. Each AE signal contains background noise. There are two categories of noises, namely, electrical noise and mechanical noise. Electrical noise includes white noise; ground loop noise; and mechanical noise, including test machine noise and friction noise, etc. In order to obtain accurate AE test results, these noise sources must be controlled. Use of a suitable "threshold" can filter out background noise, and is the prime variable that controls channel sensitivity. Gain has an important effect on energy measurements; also gain has to be set high for high-sensitivity testing.

In the current study, the threshold was set as 45dB and the gain was set as 20dB during the AE data collection. Furthermore, in order to increase the sensitivity of fracture load evaluation for study of thin films, a smaller biaxial load cell (load capacity 200 in.-lb) was installed (in addition to the original biaxial load-cell with a capacity of 10,000 in.-lb). The calibrated ratio of torque to voltage was 2.051 N-m per voltage for the smaller load-cell. A Haver sine function torque loading with displacement control was applied to the oxidized SNTT specimens. The torque voltage readout of the small load cell was set as parametric input for the LOCAN 320 system during the test. Based on the real time history of torque loading and AE signal characteristics, one can estimate the fracture load of the crack initiation event for an SNTT thin film specimen during the pure torsion test. The other information, such as rising time, duration, energy, and amplitude of AE signal, were used to identify the material zone and the crack growth characteristics of inhomogeneous materials.

5.4.2 Test Results For Oxidized SNTT Samples (Without Fatigue Pre-Cracks)

Distinct AE hits were detected during pure torsion loading cycles, as illustrated in Figs. 37-38 for non pre-cracked, U-grooved specimens Nos. 3 and 7. The related Haver sine loading cycles are shown in the top portions of Figs. 37-38. The torque limit was set to be around 60%-80% of the estimated torque that generated the maximum shear stress on the alumina scale on a 0.3 inch diameter SNTT specimen. The long spiral groove and uniform stress field distributed along the axis of the SNTT specimen provides equal opportunities for generating interfacial crack sites along the groove and at the consecutive or repetitive loading cycles. Therefore, the SNTT thin film samples were tested repeatedly under the Haver sine loading cycles.

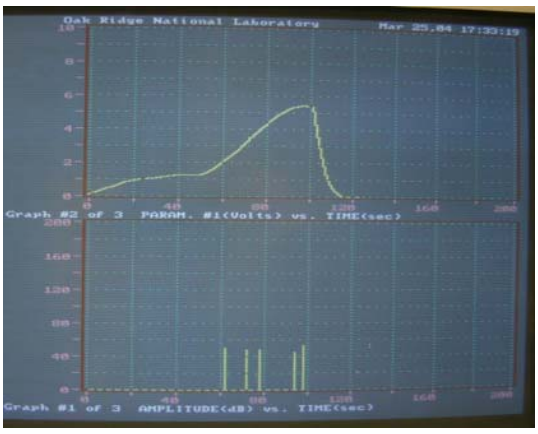

Fig. 37 Torque load (top, in volts) and AE hits (bottom) time histories for Specimen 3.

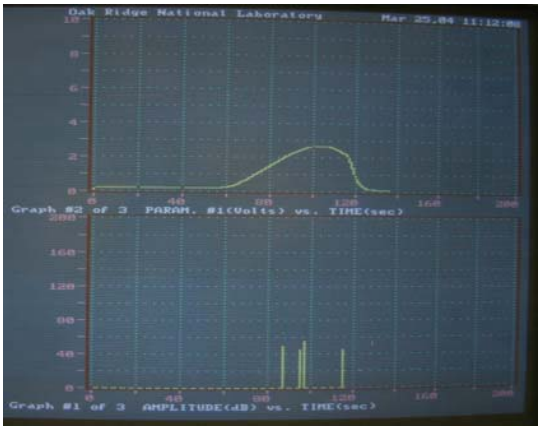

Fig. 38 Torque load (top, in volts) and AE hits (bottom) time histories for Specimen 7.

During the first three tests, few spallation sites of alumina scale were identified. However, after a series of tests, numerous spallation sites along the bottom corner of the spiral groove were revealed, and as a consequence AE hit signals became more complicated compared to those from the earlier tests. Thus, the first three torsion tests and the associated AE results were considered to be valid, and were used to estimate the fracture torque that caused the delamination of the alumina scale. The first hit of each loading cycle was considered to originate at the interface between the thin film and the substrate, assuming that the oxide-metal interface was the weakest link. The remaining hits may initiate from other interfaces, such as from the cracks associated with buckling of the scale, or from the substrate. The first three test results for

Specimen No. 3 and 7, related to the first AE hits, are listed in Table 3.

Table 3 Acoustic Emission and Torsion Test Results for Oxidized, Non pre-Cracked, U-Grooved Specimens No. 3 and 7

No. ID	Test No.	Param1 Volt	Torque N-m	Rise µs	Count	Energy	Duration µs	Amplit-ude dB
3	1	2.30	4.71	109	10	12	353	50
3	2	2.33	4.77	2	1	5	2	44
3	3	2.51	5.14	92	33	24	535	55
7	1	2.06	4.22	19	7	11	152	49
7	2	2.02	4.14	9	14	13	216	53
7	3	2.73	5.59	1	1	5	2	45

From Table 3, it can be seen that the scatter in the estimated interface fracture torque (identified from the first AE hits) was fairly small. The AE test results indicate that the proposed testing procedure is repeatable and reliable until the threshold (or maximum damage density) of the alumina scale spallation (or delamination) is reached. The test data from a high damage-density sample may provide a non-conservative or unreliable estimate of the interface toughness, due to complex AE hit response originating from numerous crack sites. Furthermore, detailed and thorough analyses may be needed to distinguish the source of these AE hits.

The energy count of AE hits can provide a very useful index for identifying the likelihood of the AE source. This is due to the fact that more energy can be stored in the substrate than in the thin film, therefore, a much larger energy count would be anticipated for AE hit sources from the substrate than from other AE hit sources. Indeed, many such AE signals were observed from the torsion loading cycles, especially for the pre-cracked SNTT samples. Furthermore, it is anticipated that less energy (or load) is required to initiate an interface crack than is required to fracture the alumina scale of high residual stress. Moreover, the AE hits initiated from an interfacial crack source underneath the thin film will have a lower energy count (or intensity) compared to a source at the fracture sites in the thin film. Therefore, the energy count of each AE hit will also provide a valuable insight regarding the source and fracture zone of crack initiation.

5.4.3 Test Results for Oxidized SNTT Samples With a Fatigue Pre-Crack

Time-history of AE hit signals from pre-cracked SNTT samples during the torsion tests are shown in Figs. 39-40.

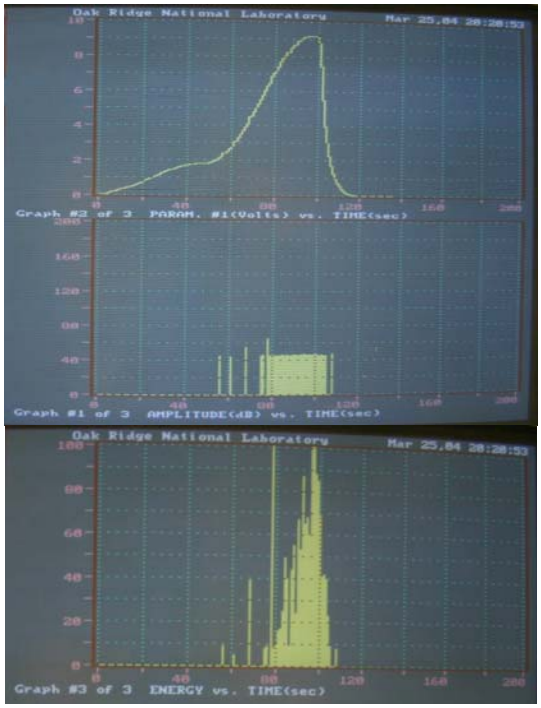

Fig.39 AE hit events from Specimen No. 1

These show significantly higher counts of AE hit and higher energy intensity that those from oxidized, non-pre-cracked SNTT specimens. In many cases, the estimated torque from the first AE hit data from the four pre-cracked samples (Specimen No. 1, 2, 5 and 9) was much lower than that obtained from the non-pre-cracked samples. This is likely to result from the rough surfaces, with numerous crack sites developing during the fatigue pre-cracking cycles. During oxidation of the SNTT samples, numerous potential flaw and anomalies can be developed at such sites, and these may fail under very low loading. The bottom portion of Figs. 39-40 is the time history of the energy counts for the AE hit events, which show that many hits had extremely high energy counts. As discussed earlier, the alloy substrate is the likely source of high energy counts, so that these probably initiated at the fatigue pre-crack sites.

Table 4 listed some of the AE test results for the pre-cracked, oxidized SNTT samples. Comparison of the data in Tables 3 and 4 indicates that non pre-cracked SNTT samples are more suitable for studying thin film interface toughness study than pre-cracked samples. On issues related to the sensitivity of these results to the groove geometry, no conclusion can be made due to lack of non-

pre-cracked V-groove thin film sample. A detailed study is needed to further evaluate the sensitivity and impact of the groove configuration to the SNTT interface toughness evaluation.

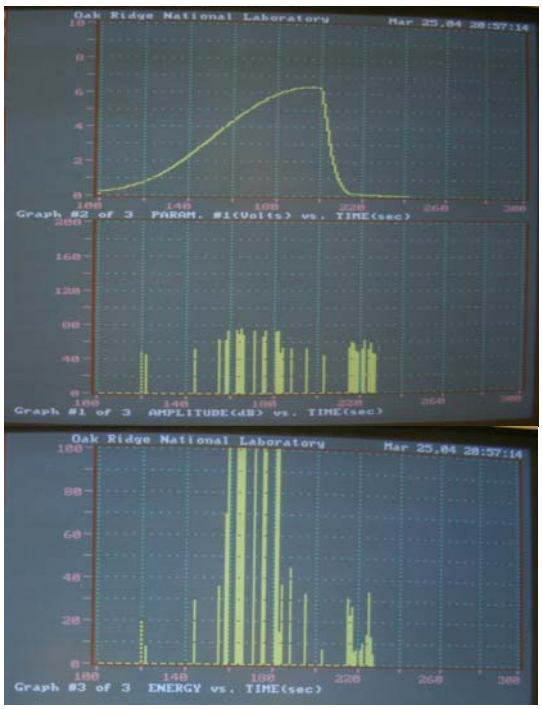

Fig.40 AE hit events from Specimen No. 5

Table 4. Acoustic Emission and Torsion Test Results for Oxidized, Pre-Cracked Specimens No. 1, 2, 5, and 9.

No. ID	Test No.	Param1 Volt	Torque N-m	Rise µs	Count	Energy	Duration µs	Ampl-itude dB
1	1	2.36	4.83	72	1	9	72	45
1	2	1.51	3.09	2	1	7	1	45
2	1	0.33	0.67	12	5	7	39	53
2	2	0.35	0.71	13	5	6	35	49
5	1	0.83	1.70	22	1	8	22	47
5	2	2.82	5.78	44	85	43	1127	59
9	1	2.63	5.39	1	1	8	1	46
9	2	0.85	1.74	10	28	17	328	53

6. Conclusions

Given the increasing reliance on the properties of thin films to provide critical functions in applications ranging from microelectronics to large propulsion and power generation equipment, and the need for procedures to ensure that such films are correctly applied, the ability to make accurate measurements of the interface strength would be a great benefit in quality control and fitness for service procedures. In addition, in applications that are critically dependent on the correct functioning of thin films and coatings, the ability to accurately measure the strength of the critical interfaces as a function of exposure to the service environment provides a basis for developing reliable lifetime models that can be used in conjunction with condition monitoring approaches to improve the security of operation of the component in question, by scheduling appropriate maintenance and avoiding unexpected failure.

This project offers an innovative testing procedure for the determination of interface fracture toughness that is applicable to thin coating materials in general. The effort included development of instrumentation, testing procedures, and analytical and finite element procedures for calculating interface fracture toughness. This new torsion bar testing procedure has been successfully developed and extended to bi-material interface fracture research. The Phase I feasibility study indicated that this approach for studying thin film interface fracture is repeatable and reliable, with much less uncertainty compared to other approaches. The demonstrated test method closely adheres to and is consistent with classical fracture mechanics theory. The evaluated J value at the interface is about 0.28 in-lb/in², and the estimated equivalence interface fracture toughness K_{IC} of MA956 is at 3.48 ksi√in, obtained from a 3-D finite element analysis. The details of the analytical evaluation of fracture toughness for the oxidized SNTT samples will be presented in the next paper.

The unique features of the testing method demonstrated are:

- The stress and strain fields produced by pure torsion of a circular bar are a function of the bar radius only, and are the same everywhere along the notch line. The length of the spiral crack is equivalent to the thickness of a compact tension specimen. The size effect that normally is a serious concern in compact-type specimens and others is virtually eliminated in SNTT specimen. Therefore, miniature specimens can be used effectively in the SNTT method.

- Fracture failure in combined mixed-mode (Mode I and Mode III) pertinent to PVP systems can be tailored for simulation studies by varying the pitch

angle of the starting notch line or, alternatively, having the standard specimen subjected to various combinations of loads in tension and torsion.

– Due to the controllable crack growth behavior and miniaturization characteristics of the SNTT technique, there is the has a potential for its use to determine the KIC values for interfaces in inhomogeneous materials, and the mechanical properties of heat-affected zones.

The SNTT technique is envisaged to offer new opportunities to promote the development of new thin film and coating materials; to provide a reliable method for use in assessing material performance; and to provide industry with a means to establish and standardize quality control. Therefore, this new approach with a main focus on measurement is expected to have wide-ranging impact on important industrial sectors and their supply chains, including power generation, construction, aerospace, automotive and electronics.

Acknowledgments

The authors gratefully acknowledge Dr. Edgar Lara-Curzio and Dr. Peter Tortorelli for their interest and support on this research. The research was sponsored by the ORNL LDRD Seed Money Program, under DOE contract DE-AC05-00OR22725 with UT-Battelle, LLC.

Reference

1. Sergey Edward Lyshevski, Nano- and Microelectromechanical Systems, CRC Press 2000, ISBN 0-8493-0916-6.
2. Marc Madou, *Fundamentals of Microfabrication*, CRC Press 1997, ISBN 0-8493-9451-1.
3. A. Maricocchi, A. bartz and D. Wortman, "PVD TBC Experience on GE Aircraft Engines," Proceedings of the Thermal Barrier Coating Workshop, NASA Lewis Research Center, NASA Conference Publication 3312, pp. 79-90, 1995.
4. Neil E. Paton, "Materials for Advanced Space Propousion Systems," Journal of Materials Science and Engineering, A143(1991), pp. 21-29.
5. Stiger, M.J., Yanar, N.M., Topping, M.G., Pettit, F.S. and Meier, G.H., *Thermal Barrier Coatings for the 21st Century.* Z. Metallk., vol. 90 (1999) p.1069-1078.
6. Miller, R.A., *Current Status of Thermal Barrier Coatings - An Overview.* Surf. & Coat. Techn., vol. 30 (1987) p.1-11.
7. Miller, R.A., *Thermal Barrier Coatings for Aircraft Engines: History and Directions.* J. Thermal Spray Technology, vol.**6** (1997) p.35-42.
8. Brindley, W.J. and Miller, R.A., *TBCs for Better Engine Efficiency.* Adv. Mater. Proc., vol.136 (1989) p.29-33.
9. Beele, W., Marijnissen, G. and van Lieshout, A., *The Evolution of Thermal Barrier Coatings - Status and Upcoming Solutions for Today's Key Issues.* Surf. & Coat. Techn., vol.121 (1999) p.61-67.
10. A.M. Karlsson, T. Xu, A.G. Evans, "The Effect Of The Thermal Barrier Coating On The Displacement Instability In Thermal Barrier Systems," Acta Materialia 50 (2002) 1211–1218.
11. Johnson C. A, Ruud J.A, Bruce R, Wortman D., Surf Coat Technology 1998;109:80–5.
12. Chaudhury, Z.A., Newaz, G.M., Nusier, S.Q., Ahmed, T. and Thomas, R.L., *Chronological Evaluation of Interfacial Damage in TBC due to Thermal Cycling.* J. Mater. Sci., vol.34 (1999) p.2475-2481.
13. Brandon, J.R. and Taylor, R., *Thermal Properties of Ceria and Yttria Partially Stabilized Zirconia Thermal Barrier Coatings.* Surf. Coat. Tech., vol.39/40 (1989) p.143-151.
14. Nesbitt, J.A., *Thermal response of various thermal barrier coatings in a high heat flux rocket engine.* Surface and Coatings Technology, vol.43 (1990) p.458-469.
15. Zhu, D.M. and Miller, R.A., *Thermal Conductivity and Elastic Modulus Evolution of Thermal Barrier Coatings under High Heat Flux Conditions.* J. Ther. Spray Techn., vol.**9** (2000) p.175-180.
16. Ray, A.K., *Failure Mode of Thermal Barrier Coatings for Gas Turbine Vanes under Bending.* Int. J. Turbo Jet Eng., vol.**17** (2000) p.1-24.
17. Pint, B.A., Wright, I.G., Lee, W.Y., Zhang, Y., Prüssner, K. and Alexander, K.B., *Substrate and Bond Coat Compositions: Factors Affecting Alumina Scale Adhesion.* Mat Sci & Eng A, vol.245 (1998) p.201-211.
18. Pindera, M.J., Aboudi, J. and Arnold, S.M., *The Effect of Interface Roughness and OxideFilm Thickness on the Inelastic Response of Thermal Barrier Coatings to Thermal Cycling.* Mat. Sci. & Eng. A, vol.284 (2000) p.158-175.
19. Evans, A.G., Hutchinson, J.W. and He, M.Y., *Micromechanics Model for the Detachment of Residually Compressed Brittle Films and Coatings.* Acta. Mater., vol.47 (1999) p.1513-1522.

20. M. L. William, 1959, "The Stress Around a Fault or Crack in Dissililar Media," Bull. Seismol. Soc. America, vol. 49, pp. 199-204.
21. F. Erdogan, 1965, "Stress Distribution in Bounded Dissimilar Materials with Cracks," J. App. Mech., vol. pp. 403-410.
22. D. B. Bogy, 1971. "Two edge-bonded elastic wedge of different materials and wedge angles under surface traction," *J of Applied Mechanics*, Vol. 38, pp377-386.
23. J. R. Rice, "Elastic fracture mechanics concepts for interfacial cracks," *JAM*, 1988.
24. C. F. Shih, "Cracks on bimaterial interfaces: elasticity and plasticity aspects", MSE, 1991.
25. Hutchinson, J. W. and Suo, Z., 1992. "Mixed Mode Cracking in Layered Materials," *Advances in Applied Mechanics*. Vol. 29, pp. 63-191.
26. Rice, J. R., Suo, Z., and Wang, J.-S. (1990). "Mechanics and thermodynamics of brittle interfacial failure in bimaterial systems." *Acta-Scripta Metallurgica Proceedings Series*, M. Ruhle, A. G. Evans, M. F. Ashby, and J. P. Hirth, eds., Pergamon Press, Oxford, 269-294.
27. Turner, M. R., and Evans, A. G. (1996). "An experimental study of the mechanisms of crack extension along an oxide/metal interface." *Acta mater.*, 44(3), 863-871.
28. P. G. Charalambides, J. Lund, A. G. Evans, and R. M. McMeeking, "A Test Specimen for Determining the Fracture Resistance Bimaterial Interface," Journal of Applied Mechanics, Vol. 55, pp. 77-82, March 1989.
29. Z. Suo and J.W. Hutchinson, "Sandwich Test Specimens for Measuring Interface Crack Toughness," *Mater. Sci. Engeg.*, A 107 (1989), pp. 135-143.
30. M. J. Stiger, L. A. Ortman, F. S. Pettie and G. H. Meier, "Measurement of Interfacial Toughness in Thermal Barrier Coating System by Indentation," ASTM Annual Program Review, November 1999.
31. Junlan Wang, Richard L. Weaver, Nancy R. Sottos, "A Parametric Study of Laser Induced Thin Film," Journal of Experimental Mechanics, Vol 42, No. 1, march 2002, pp. 74-83.
32. V. Gupta, A. S. Argon, J. A. Cornie, and D. M. Parks, "Measurement of Interface Strength by a Laser Spallation Technique," J. Mech. Phys. Solids, vol. 40, 141-180 (1992).
33. J. A. Wang, K. C. Liu, D. E. McCabe, and S. A. David, "An Innovative Small Specimen Testing Technique for the Determination of Fracture Toughness," ORNL/M-6366, 1999.
34. J. A. Wang, K. C. Liu, D. E. McCabe, and S. A. David, "Using Torsion Bar Testing to Determine Fracture Toughness, K_{IC}," *Journal of Fatigue & Fracture for Engineering Materials and Structure*, Vol. 23, pp 45-56, 2000.
35. J. A. Wang, "TOR3D-KIC: A 3-D Finite Element Analysis Code for Determination of Fracture Toughness, K_{Ic}, for Spiral Notch Torsion Fracture Test (SNTT)," ORNL LTR Report, 2001.
36. J. A. Wang, K. C. Liu, and D. E. McCabe, "An Innovative Technique for Measuring Fracture Toughness of Metallic and Ceramic Materials," *Fatigue and Fracture Mechanics*: 33rd Volume, *ASTM STP 1417*, W. G. Reuter and R. S. Piascik, Eds., 2002.
37. J. A. Wang, K. C. Liu, and G. A. Joshi, "Using Torsion Bar Testing to Determine Fracture Toughness of Ceramic Materials," *ASME Proceeding of ETCE 2002 Conference on Composite Materials Design & Analysis*, February 3-4, 2002, Houston, Texas.
38. Jy-An John Wang, "Oak Ridge National Laboratory Spiral Notch Torsion Test System," Journal of *Practical Failure Analysis*, Vol. 3(4) August 2003.
39. J. A. Wang and K. C. Liu, "A New Approach To Evaluate Fracture Toughness of Structural Materials," Proceedings of ASME 2003 Pressure Vessel and Piping, July 2003.